Analysis of satellite and in situ ground deformation data integrated by the SISTEM approach: The April 3, 2010 earthquake along the Pernicana fault (Mt. Etna - Italy) case study

Christian Bignami, Alessandro Bonforte, Pierre Briole, Francesco Obrizzo, Giuseppe Puglisi, Salvatore Stramondo, Urs Wegmüller

Earth and Planetary Science Letters xxx (2011) xxx–xxx

Contents lists available at SciVerse ScienceDirect

Earth and Planetary Science Letters

journal homepage: www.elsevier.com/locate/epsl

Analysis of satellite and in situ ground deformation data integrated by the SISTEM approach: The April 3, 2010 earthquake along the Pernicana fault (Mt. Etna - Italy) case study

Francesco Guglielmino [a,*], Christian Bignami [b], Alessandro Bonforte [a], Pierre Briole [c], Francesco Obrizzo [d], Giuseppe Puglisi [a], Salvatore Stramondo [b], Urs Wegmuller [e]

[a] Istituto Nazionale di Geofisica e Vulcanologia, Oss. Etneo - Sezione di Catania, P.zza Roma 2, Catania, Italy
[b] Istituto Nazionale di Geofisica e Vulcanologia, Remote Sensing Laboratory, Centro Nazionale Terremoti, Vigna Murata, Rome, Italy
[c] Ecole Normale Supérieure, Laboratoire de Géologie, UMR-CNRS 8538, 24 Rue Lhomond, 75005 Paris, France
[d] Istituto Nazionale di Geofisica e Vulcanologia, Oss. Vesuviano, v. Diocleziano 328, Napoli, Italy
[e] GAMMA Remote Sensing, CH-3073 Gümligen, Switzerland

ARTICLE INFO

Article history:
Received 26 June 2011
Received in revised form 12 October 2011
Accepted 15 October 2011
Available online xxxx

Keywords:
DInSAR
GPS
leveling
multidisciplinary approach
ground deformation

ABSTRACT

Etna is known worldwide as one of the most studied and monitored active volcanoes. Flank instability along the eastern and southern portions of Mt. Etna has been observed and measured thanks to geodetic networks and InSAR data analysis. The spreading area is bordered to the north by the east–west Pernicana Fault System (PFS) whose dynamics is often linked with the eruptive activity, as recently observed during the 2002–2003 eruption.

A seismic sequence occurred from April 2–3, 2010, along the PFS with very shallow (a few hundred meters) mainshocks of magnitude 4.3 and 3.6. Explosions and ash emissions at the summit craters followed this swarm culminating a few days later (April 7–8). Despite their small magnitude, the earthquakes caused damage and significant surface fracturing along the PFS.

In order to investigate and measure the deformations in the near field of the earthquakes, the SISTEM integration approach has been exploited. The SISTEM enabled integrating geodetic in situ ground deformation measurements (GPS and leveling) with satellite interferometric measurements (ENVISAT and ALOS), in order to obtain high resolution 3D displacement maps, allowing to overcome the limitations of each technique and take advantage of the particular features of each of them. The integrated ground deformation field evidenced that the medium behave elastically.

We inverted the SISTEM results using an optimization algorithm based on the Genetic Algorithm (GA) in order to model the kinematics of the PFS associated to seismic swarm; the results are in good agreement with the field evidence and improved the knowledge on the kinematics of the PFS and Mt. Etna's unstable flank.

1. Introduction

Mt. Etna is a 3300 m high and ~40×60 km wide volcano, formed in the last 200 Ka (Branca et al., 2008; Corsaro and Mazzoleni, 2002; Romano, 1982, and references therein). The volcano lies on the eastern coast of Sicily, and it is characterized by a structural setting resulting from a complex regional tectonic with a compressive regime along a near N-S trend and an extensional regime oriented approximately E-W that is observable along the eastern coast of Sicily (see Bousquet and Lanzafame, 2004).

The eastern flank of the volcanic edifice shows a fairly continuous seaward motion, due to the interrelationship between gravity instability and magma intrusion (e.g. Bonforte and Puglisi, 2003, 2006; Bonforte et al., 2011; Borgia et al., 1992; Obrizzo et al., 2001; Puglisi et al., 2008).

The Pernicana Fault System (PFS) is considered as the northern border of this sliding eastern flank of Mt. Etna. The PFS is one of the most active tectonic structures in the Etna area and has been studied thoroughly in the recent decade (Acocella and Neri, 2005; Azzaro et al., 2001; Bonforte et al., 2007a; Currenti et al., 2010; Neri et al., 2004; Palano et al., 2006).

The PFS is composed of discrete segments (Fig. 1), arranged in a right stepping en-èchelon configuration, forming a near continuous E-W left lateral shear zone. It develops from the North-East Rift eastwards crossing the Piano Provenzana, Piano Pernicana, and the Rocca Campana area; at the eastern end the morphological evidence disappears, and the fault can be detected only by creep-induced damage to manmade features along the dislocation lines.

* Corresponding author. Tel.: +39 0957165809.
E-mail address: francesco.guglielmino@ct.ingv.it (F. Guglielmino).

0012-821X/$ – see front matter © 2011 Elsevier B.V. All rights reserved.
doi:10.1016/j.epsl.2011.10.028

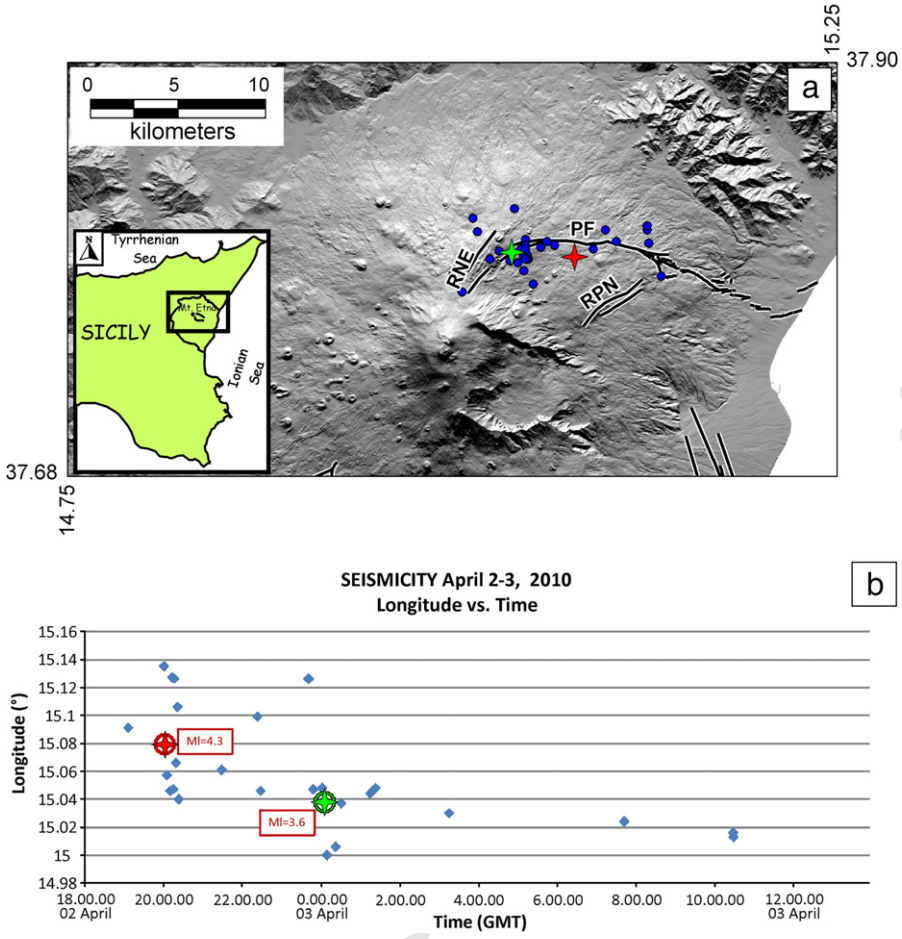

Fig. 1. (a) Structural outline of Mt. Etna reporting main faults known from geological surveys; RNE = NE-rift; PF = Pernicana fault; RPN = Ripe della Naca faults; the blue circles represent the epicenter of the earthquakes occurring between 02 and 03 April (Gruppo Analisi Dati Sismici, 2010); the main shocks (Ml = 4.3 and Ml = 3.6) with a red and a green star respectively are reported. Bottom left and upper right corner coordinates are in decimal degree WGS84 datum. (b) In the bottom panel, the seismicity recorded between 02 and 03 April along the PFS is reported. The plot represents the longitude of the earthquake epicenters versus time. (For interpretation of the references to color in this figure legend, the reader is referred to the web version of this article.)

This structure shows a constant and continuous eastward motion at a rate of about 2 cm/year, mainly related to the gravitational spreading of the eastern flank that is occasionally accelerated by volcanic activity (Bonforte et al., 2007a); it is characterized by continuous seismic movements associated with the eastern flank sliding, while shallow (<2 km) seismic activity (2<M<3.5) sometimes accompanies the surface deformation along the central and western portion of the PFS (Azzaro et al., 1998; Bonforte et al., 2007b). The Mt. Etna leveling network has permitted the study and monitoring of the PFS since 1980, highlighting that the fault slips almost homogeneously over a large time scale, with a kinematic according to listric southward dipping fault (Obrizzo et al., 2004).

Between April 2nd and 3rd 2010, an earthquake swarm took place along the central part of the PFS, accompanied by ground fracturing with left lateral movement of about 0.5 m, propagating from east to west from the PFS area and then migrating to the eastern NE Rift.

Between 19.06 GMT on April 2nd and 07.42 GMT, April 3rd 2010, a seismic swarm (about 170 earthquakes recorded) took place along the central part of the PFS (Langer, 2010), accompanied by ground fracturing with left lateral movement of about 0.5 m, propagating from east to west from the PFS area and then migrating to the eastern NE Rift. All the earthquakes were very shallow (depth <1 km) and the main shocks (M4.3 and M3.6) were recorded at 20.04 GMT on April 2nd and at 00:05 GMT, April 3rd respectively, in the Villaggio Turistico Mareneve area. In this work, different geodetic datasets coming from different techniques are analyzed in order to figure out image the ground deformation pattern associated with this seismic swarm.

2. Data

The analysis of the ground deformation pattern associated with the seismic swarm, was performed by integrating the in situ data with available interferometric measurements, coming from the Synthetic Aperture Radar (SAR) data acquired by ALOS and ENVISAT satellites.

2.1. In situ ground deformation data

2.1.1. GPS networks and surveys

Immediately after the earthquakes, a specific GPS survey was planned on part of the GPS monitoring network of Mt. Etna on the NE side of the volcano, including also two small sub-networks, aimed at monitoring the central section of the PFS (Bonforte et al., 2007a, 2007b). During this survey, some GPS stations were installed on the self-centering benchmarks belonging to the main GPS monitoring network of the volcano, collecting data at 30 s rate during 24 h static sessions from April 13 (DOY 103) to April 20 (DOY 110). The data from these stations were then processed together with those collected by the permanent GPS network of Mt. Etna, in order to insert the surveyed network into a wider reference covering the entire volcano. The comparison between the results of this survey with those of the previous campaign, carried out in June 2009 (at

Please cite this article as: Guglielmino, F., et al., Analysis of satellite and in situ ground deformation data integrated by the SISTEM approach: The April 3, 2010 earthquake along th..., Earth Planet. Sci. Lett. (2011), doi:10.1016/j.epsl.2011.10.028

either periodic or permanent stations) revealed the 3D ground deformation pattern of the volcano (see Fig. 2), with a higher detail on the whole northeastern flank of Mt. Etna. In this period, ground displacements of the GPS network highlighted a general inflation of the volcano, evidenced by the slight uplift and radial pattern of the vectors on the southern, western and northern sides of the edifice. As already highlighted by previous works (Bonforte and Puglisi, 2003; Houlie et al., 2006; Puglisi and Bonforte, 2004), the eastern flank shows an independent pattern with subsidence and stronger horizontal displacements due to its continuous seawards motion. In particular, from July 2009 to April 2010, the ground deformation pattern on this unstable sector of the volcano was unusually strong; indeed, horizontal displacements of about 5–6 cm were measured at all stations located along the NE Rift-PFS as well as on the entire north-eastern and lower eastern flanks of the volcano. The horizontal vectors show a significant rotation of the azimuth, from NE-ward on the upper part to SE-ward on the lower flank, testifying about the driving effect played by the PFS in the general seaward motion; furthermore, the decoupling role of the PFS is certified by the sharp decay of the deformation from benchmark RPN5 to benchmark RPN1, only 800 m far from the northern side of the fault (see Fig. 2).

2.1.2. Leveling route and surveys

During the GPS survey, on April 2010, the Pernicana segment of the leveling network was also surveyed in order to achieve the most accurate sampling of the vertical ground deformation field. The measured leveling route is 11 km long and consists of 39 benchmarks which perpendicularly crosses the Pernicana fault trace at an altitude of about 1400 m asl (Fig. 3) (Obrizzo et al., 2001, 2004).The leveling line crossing the PFS has a higher density of points, near the geological structure, for allowing the detailed study of the observed displacement field. The benchmarks are made by steel or brass and generally consolidated either directly into solid lava outcrops or into concrete foundation. Surveys were carried out with an electronic Leica DNA03 and an optical Wild NA2 levels and we used the double-run precise leveling method in order to achieve the maximum precision in the vertical position of the benchmarks, with a mean error less than 1.0 mm/km$^{1/2}$. 19 of the 39 benchmarks were measured during two leveling surveys carried out in November 2009 and April 2010 along the Pernicana leveling route. The reference benchmark used to calculate the height variations is the 73A-B benchmark (Casa Pitarrone), which lies on the northern side of the fault at a distance of about 1 km from it.

In this 5-month comparison, the benchmarks lying on the northern side of the fault show an uplift, suddenly interrupted by a jump of about 70 mm affecting the stations across the fault (77B and 78A benchmarks), due to the earthquake. On the southern side of the fault, the benchmarks lying just south of the structure showed a subsidence of about 15 mm due to the continuous and independent seaward sliding of the eastern flank of Mt. Etna (Bonforte et al., 2008). We highlighted here that in the area close to the fault, where the high vertical deformation was recorded, the medium seems to behave elastically, confirmed by the opposite motion of the two sides of the fault..

2.2. DInSAR satellite data

Seeking to investigate the deformation occurring along the PFS during the events of April 3rd 2010, we performed a DInSAR (Differential Interferometry Synthetic Aperture Radar) analysis of ascending and descending ENVISAT-ASAR, and of ascending ALOS-PALSAR images encompassing the date of the earthquake.

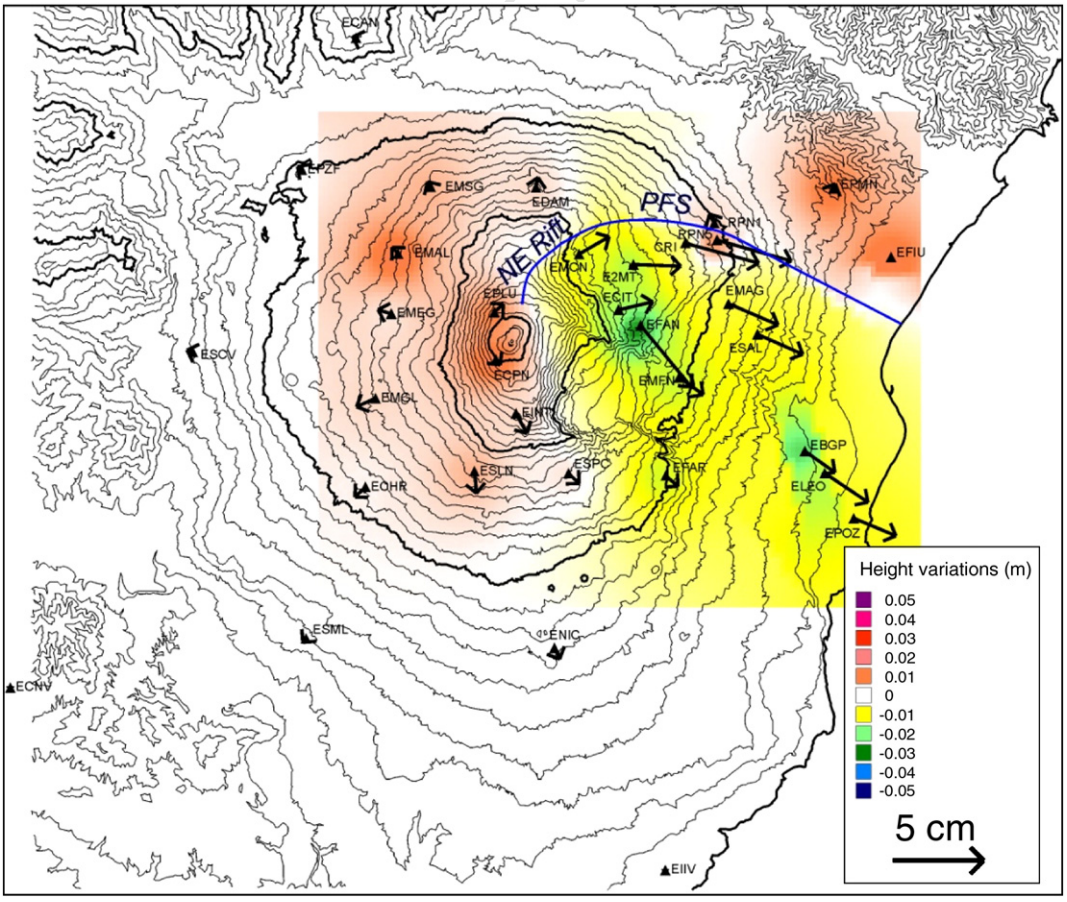

Fig. 2. Displacement vectors and height variations from the comparison between June 2009 and April 2010. The arrows represent the horizontal displacement vectors, while the vertical displacement value is presented by a color map obtained by interpolating the measurements relative to each benchmark.

Please cite this article as: Guglielmino, F., et al., Analysis of satellite and in situ ground deformation data integrated by the SISTEM approach: The April 3, 2010 earthquake along th..., Earth Planet. Sci. Lett. (2011), doi:10.1016/j.epsl.2011.10.028

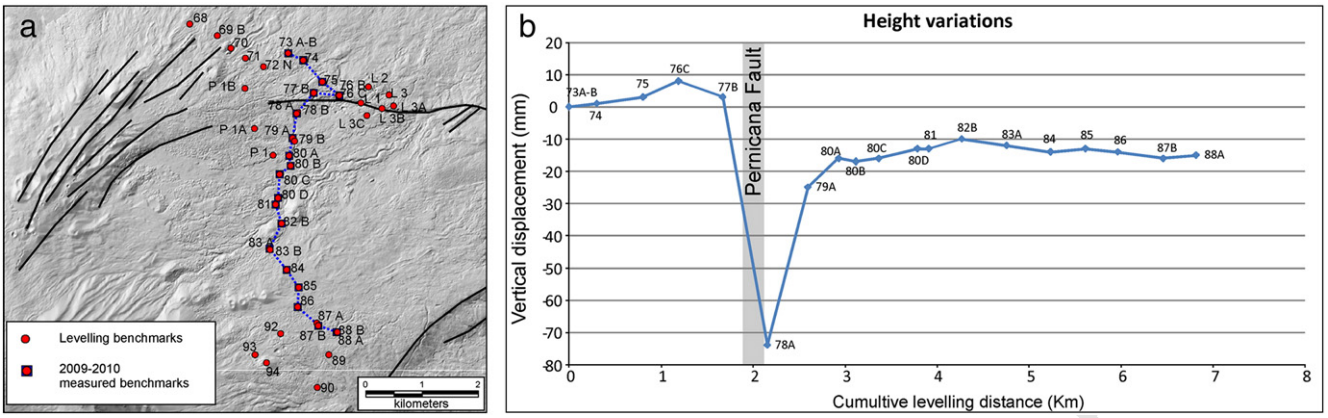

Fig. 3. Pernicana leveling network operating on Mt. Etna (a), the main structural features are reported in black, the blue dashed line represents the segment of the leveling route surveyed in 2009 and 2010. (b) Height variations measured from November 2009 to April 2010; the gray area represents the fault trace crossing the profile. (For interpretation of the references to color in this figure legend, the reader is referred to the web version of this article.)

The procedure used for the generation of interferometric products was the so-called "two-pass interferometry" (Massonnet and Feigl, 1998). This method requires two SAR images to generate a real phase interferogram that is correlated with topography and changes in topography. To analyze the topographical displacements, the topography-dependent part of the interferogram should be eliminated by using an external DEM (Digital Elevation Model). The SAR satellite data have better spatial resolution with respect to in situ geodetic measurements, even if the accuracy of the DInSAR measurements is about one order of magnitude lower due to the orbit errors, to the DEM accuracy and atmospheric artifacts. The DInSAR ground deformation measurements are able to detect the 1D displacements along the Line of Sight (LOS) of the sensor, and this kind of measurement does not allow the real ground displacement to be imaged.

We took advantage of the available data acquired by different SAR sensors on board the ENVISAT and ALOS platform, with different viewing angles and different acquisition geometries on ascending and descending orbits. This dataset allowed us, to better image the ground deformation which occurred in the coseismic period.

2.2.1. Envisat data

ENVISAT is the European ESA spacecraft equipped with the ASAR C-band sensor (5.3 GHz with a wavelength of 5.6 cm), acquiring data over Mt. Etna on both ascending and descending orbits with a revisiting time of 35 days.

We chose a time window consistent with the leveling data, that also allowed avoiding the decorrelation due to the snow coverage affecting the volcano in the winter time. We analyzed an ascending pair related to 07/10/2009–05/05/2010 period and a descending pair related to 18/11/2009–07/04/2010 time interval. We processed these data using the Jet Propulsion Laboratory (JPLs)/Caltech Repeat Orbit Interferometry Package (ROI_PAC, version 3.0) (Rosen et al., 2004).

The ENVISAT images (Fig. 4) show the general seaward movement of the eastern flank of Mt. Etna well. They also show very intense but local LOS displacements (about three fringes) on the ENVISAT ascending interferogram and a lower variation for the descending geometry, on the hanging wall area close to the PFS trace. Here, the strong ground deformation gradient produces the decorrelation in the ascending image, indicating that the LOS displacement between adjacent pixels is higher than 1 wavelength.

Conversely, the footwall area close to the PFS trace (northern side of the fault), approaches to the sensor on the ascending geometry while LOS displacement is not detected by the descending pair. The differences in the LOS displacements between ascending and descending geometry, are probably due to the oblique normal/left-lateral kinematics of the PFS (as deduced also by GPS and leveling data); indeed, both vertical (lowering) and horizontal (eastward) components of motion on the southern side of the fault, produce a strong lengthening of the LOS distance for ascending geometry, while the two components act in opposite ways for the descending geometry,

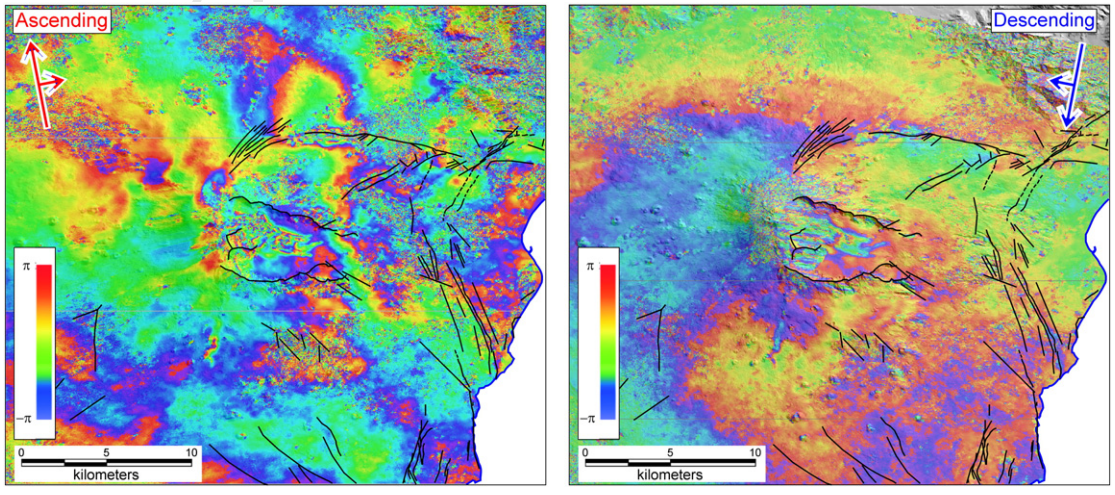

Fig. 4. (a) Ascending ENVISAT interferogram referring to 07/10/2009–05/05/2010 and (b) the ENVISAT descending interferogram of the 18/11/2009–07/04/2010 time interval.

Please cite this article as: Guglielmino, F., et al., Analysis of satellite and in situ ground deformation data integrated by the SISTEM approach: The April 3, 2010 earthquake along th..., Earth Planet. Sci. Lett. (2011), doi:10.1016/j.epsl.2011.10.028

resulting in lower LOS distance variations compared to the ascending data set (see Fig.S1 supplementary materials). In the same way, on the northern side, an uplift coupled with a westward motion, produce LOS shortening in the ascending view but almost no variation in the descending one.

In order to compare the SAR data with the in situ measurements, we extracted LOS displacements of those pixels closest to the leveling benchmarks; in Fig. 5 the vertical displacements measured by leveling are plotted together with the ascending LOS displacements of their nearest pixels. The plot shows a very good agreement between the two datasets, and as expected the magnitude of the LOS displacements is higher due to the contribution of the eastward motion of the southern side of the fault. Finally, both leveling and DInSAR data confirm that an intense local deformation episode occurred very close to the PFS, affecting a narrow strip (500 m) along the southern side of the fault.

2.2.2. ALOS data

We exploited the data acquired by PALSAR (Phase Array type L-band Synthetic Aperture) on board the Japanese ALOS (Advanced Land Observation Satellite) platform. PALSAR is an L-band (1.27 GHz, corresponding to 23.6 cm wavelength) SAR sensor, with high resolution capabilities. Thanks to its carrier frequency and spatial resolution, PALSAR is less affected by loss of complex correlation due to temporal and spatial baselines, which reflects in more coherent interferograms.

Two frames covering two adjacent tracks (track 637 and 638) were used, both along ascending path. Concerning the track number 638, the images were taken on February 21 and April 8, while for the track 637, the scenes have been acquired on March 22 and May 7 2010. All the images except the one acquired in May 2010, are Fine Beam Single (FBS) polarization images, i.e. HH polarization at about 9 m resolution in range and 4 m in azimuth. The May 7th scene is a Fine Beam Dual (FBD) polarization, i.e. HH and HV polarizations with the same resolution in azimuth and double resolution (18 m) in range with respect to FBS.

The deformation field has been retrieved by applying a two-pass DInSAR processing using GAMMA software.

In order to exploit the high resolution of PALSAR and the typical high coherence of L-band, especially with these low perpendicular baselines (178 m and 133 m for tracks 637 and 638 respectively), the interferograms have been derived at a resolution of 25 m per pixel. The phase contribution of height dependent atmospheric delay, has been estimated and removed. To avoid a misinterpretation of deformation over the volcano the estimation was done over the hills to the south and north of Etna using a linear model. In order to further reduce the interferometric phase noise, the interferograms have been adaptively filtered (Goldstein and Werner, 1998). The

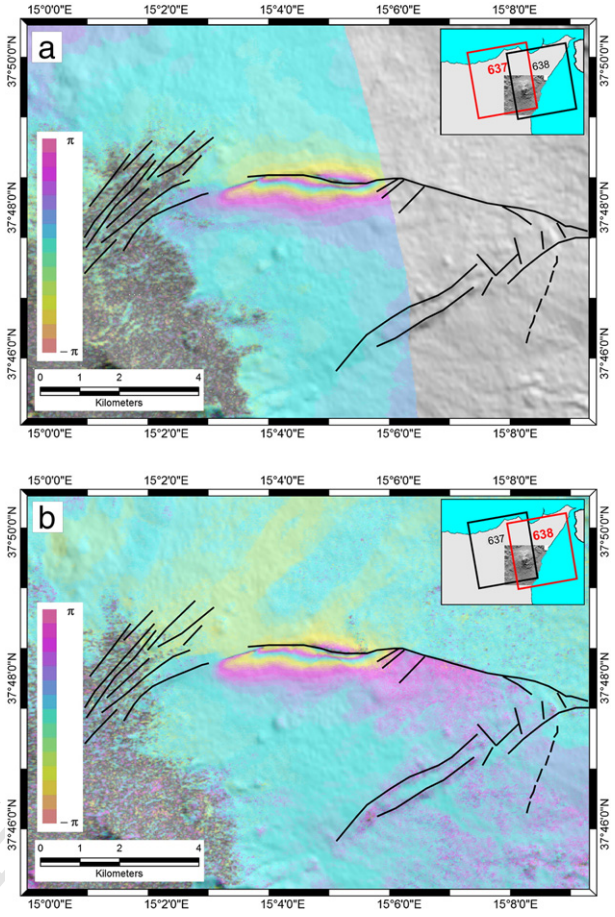

Fig. 6. (a) The resulting L-band interferograms for track 637, and (b) for track 638. The upper right box show the ALOS-PALSAR frames superimposed on the map of the Etna area.

position of the two frames with respect to the PFS with the results for both tracks, are shown in Fig. 6.

It is worth noting that the deformation patterns, i.e. the fringe number, are the same for the two tracks. In particular, a maximum of two fringes can be counted close to the PFS fracture, which means, at L band, that a deformation of about 23 cm in the LOS of PALSAR (i.e. about 38 incidence angle), has been measured.

On the northern side of the PFS area an uplift is visible which confirms the fault kinematic already evidenced by ENVISAT ascending and leveling datasets. This movement toward the sensor has a

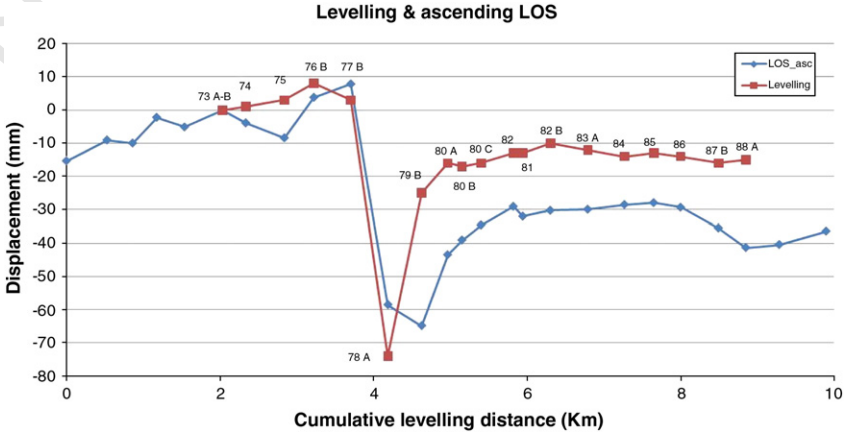

Fig. 5. Comparison between vertical displacement measured by leveling and ascending LOS distance variations measured by ENVISAT.

Please cite this article as: Guglielmino, F., et al., Analysis of satellite and in situ ground deformation data integrated by the SISTEM approach: The April 3, 2010 earthquake along th..., Earth Planet. Sci. Lett. (2011), doi:10.1016/j.epsl.2011.10.028

minor extent with respect to the ENVISAT ascending data, probably due to the geometry because ALOS has a higher incidence angle compared to ENVISAT.

From this analysis we highlight that both L-band ALOS images confirmed a strong ground deformation in the near field of the fault, rapidly decreasing on moving away from it. This pattern is not imaged by ENVISAT ascending data because it exceeds the ASAR maximum detectable deformation gradient for C-band frequency, which is 1.4 cm per pixel according to Massonnet and Feigl (1998). Furthermore, it is possible to affirm that the LOS deformation of about 23 cm, detected by ALOS, is due mainly to the horizontal component because the maximum vertical displacement measured by leveling data is only of 7 cm.

3. Integration of heterogeneous data: SISTEM approach

In order to investigate the ground deformation pattern in its 3D components (east, north and up) associated with this event, an application of the novel SISTEM (Simultaneous and Integrated Strain Tensor Estimation from geodetic and satellite deformation measurements) approach proposed by (Guglielmino et al., 2011) is here presented. To achieve higher accuracy and get better constraints on the 3D components of the displacements, we improved the standard formulation of SISTEM approach, originally based on the GPS and a single DInSAR sensor, in order to take into account all the available datasets (GPS, leveling, ascending and descending ENVISAT C-band interferograms and the ALOS L-band data).

In the following, we describe briefly the mathematical background of the SISTEM approach.

Let us assume that a geodynamic process (e.g. an earthquake) deforms a portion of the Earth's surface; according to small deformation theory, we define an arbitrary point P, having position $x_0 = (x_{10}, x_{20}, x_{30})$, and N surrounding experimental points (EPs) whose positions and displacements are respectively $x_{(n)} = (x_{1(n)}, x_{2(n)}, x_{3(n)})$ and $u_{(n)} = (u_{1(n)}, u_{2(n)}, u_{3(n)})$ where $n = 1..N$. Under such a hypothesis, adopting a linear approach, the problem of estimating the displacement components U_i ($i = 1..3$) of the point P, from the experimental data $u_{(n)} = (u_{1(n)}, u_{2(n)}, u_{3(n)})$, can be modeled by the N equations [Teza et al. 2008]:

$$u_{i(n)}(x) = H_{ij}\Delta^{ij}x_{j(n)} + U_i(i,j = 1..3) \tag{1}$$

where $\Delta x_{j(n)} = x_{j(n)} - x_{j0}$ are the components of the vector distance between the n^{th} EP experimental points and the arbitrary point P, while $H_{ij} = \partial ui/\partial xi$ are the elements of the displacement gradient tensor. In (1) the matrix H can be broken down into a symmetric and an anti-symmetric part as $H = E + \Omega$, where E is the Strain Tensor and Ω is the rigid body rotation tensor.

A number K of InSAR interferograms can be related to the components of the displacement vector of an arbitrary point P according to the following equation:

$$D_{LOS}^{SP} = [U_1, U_2, U_3]\left[S_x^{SP}, S_y^{SP}, S_z^{SP}\right]^T (S = 1..K) \tag{2}$$

where D_{LOS}^{SP} is the S^{th} known LOS displacement of the point P and $\left[S_x^{SP} S_y^{SP} S_z^{SP}\right]$ is the unit vector pointing from the point P toward the S^{th} satellite acquisition.

In order to integrate GPS, InSAR and leveling dataset, we resolve a linear system of the kind $Al = u$ using the Weighted Least Squares (WLS) approach, where the Design Matrix **A**, the Observation vector **u**, and the column vector of unknown parameters **l** are defined as follows:

$$A = \begin{bmatrix}
1 & 0 & 0 & \Delta x_{1(1)} & \Delta x_{2(1)} & \Delta x_{3(1)} & 0 & 0 & 0 & 0 & \Delta x_{3(1)} & -\Delta x_{2(1)} \\
0 & 1 & 0 & 0 & \Delta x_{1(1)} & 0 & \Delta x_{2(1)} & \Delta x_{3(1)} & 0 & -\Delta x_{3(1)} & 0 & \Delta x_{1(1)} \\
0 & 0 & 1 & 0 & 0 & \Delta x_{1(1)} & 0 & \Delta x_{2(1)} & \Delta x_{3(1)} & \Delta x_{2(1)} & -\Delta x_{1(1)} & 0 \\
\cdot & \cdot & \cdot & \cdot & \cdot & \cdot & \cdot & \cdot & \cdot & \cdot & \cdot & \cdot \\
\cdot & \cdot & \cdot & \cdot & \cdot & \cdot & \cdot & \cdot & \cdot & \cdot & \cdot & \cdot \\
\cdot & \cdot & \cdot & \cdot & \cdot & \cdot & \cdot & \cdot & \cdot & \cdot & \cdot & \cdot \\
1 & 0 & 0 & \Delta x_{1(N)} & \Delta x_{2(N)} & \Delta x_{3(N)} & 0 & 0 & 0 & 0 & \Delta x_{3(N)} & -\Delta x_{2(N)} \\
0 & 1 & 0 & 0 & \Delta x_{1(N)} & 0 & \Delta x_{2(N)} & \Delta x_{3(N)} & 0 & -\Delta x_{3(N)} & 0 & \Delta x_{1(N)} \\
0 & 0 & 1 & 0 & 0 & \Delta x_{1(N)} & 0 & \Delta x_{2(N)} & \Delta x_{3(N)} & \Delta x_{2(N)} & -\Delta x_{1(N)} & 0 \\
0 & 0 & 1 & 0 & 0 & \Delta x_{1(1)} & 0 & \Delta x_{2(1)} & \Delta x_{3(1)} & \Delta x_{2(1)} & -\Delta x_{1(1)} & 0 \\
\cdot & \cdot & \cdot & \cdot & \cdot & \cdot & \cdot & \cdot & \cdot & \cdot & \cdot & \cdot \\
0 & 0 & 1 & 0 & 0 & \Delta x_{1(M)} & 0 & \Delta x_{2(M)} & \Delta x_{3(M)} & \Delta x_{2(M)} & -\Delta x_{1(M)} & 0 \\
S_x^{(1)P} & S_y^{(1)P} & S_z^{(1)P} & 0 & 0 & 0 & 0 & 0 & 0 & 0 & 0 & 0 \\
\cdot & \cdot & \cdot & \cdot & \cdot & \cdot & \cdot & \cdot & \cdot & \cdot & \cdot & \cdot \\
S_x^{(K)P} & S_y^{(K)P} & S_z^{(K)P} & 0 & 0 & 0 & 0 & 0 & 0 & 0 & 0 & 0
\end{bmatrix} \tag{3}$$

$$u = \left[u_{1(1)} u_{2(1)}\ u_{3(1)} \ldots u_{1(n)} u_{2(n)}\ u_{3(n)}\ \ u_{3(1)} \ldots u_{3(M)}\ D_{LOS}^{1P} \ldots D_{LOS}^{KP}\ \right]^T \tag{4}$$

$$l = [U_1 U_2 U_3 \varepsilon_{11} \varepsilon_{12} \varepsilon_{13} \varepsilon_{22} \varepsilon_{23} \varepsilon_{33} \omega_1 \omega_2 \omega_3]^T \tag{5}$$

Please cite this article as: Guglielmino, F., et al., Analysis of satellite and in situ ground deformation data integrated by the SISTEM approach: The April 3, 2010 earthquake along th..., Earth Planet. Sci. Lett. (2011), doi:10.1016/j.epsl.2011.10.028

where ε_{ij} are the components of the strain tensor E defined as:

$$E = \begin{bmatrix} \varepsilon_{11} & \varepsilon_{12} & \varepsilon_{13} \\ \varepsilon_{12} & \varepsilon_{22} & \varepsilon_{23} \\ \varepsilon_{13} & \varepsilon_{23} & \varepsilon_{33} \end{bmatrix} \tag{6}$$

and ω_i are the components of the rigid body rotation tensor Ω defined as:

$$\Omega = \begin{bmatrix} 0 & -\omega_3 & \omega_2 \\ \omega_3 & 0 & -\omega_1 \\ -\omega_2 & \omega_1 & 0 \end{bmatrix} \tag{7}$$

It should be observed that the A matrix consists of 3 N + M + K rows : the first 3 N rows can be viewed as N blocks of three equations which represent information on the position of each GPS benchmark with respect to the arbitrary point P; similarly the M equations refer to leveling benchmarks, while the last K equations refer to the corresponding DInSAR data. A detailed description of the WLS solution of the proposed linear system is reported in Guglielmino et al., (2011).

The heterogeneous dataset that we analyzed in the previous sections, ranging over a different time span, and having different spatial resolution, was able to image the coseismic displacement due to the earthquakes, except for the GPS data. In fact, the GPS dataset, covering June 2009–April 2010 time span, well depicted the ground deformation occurred on Mt. Etna, evidencing the eastward movement of its eastern flank, but it is not able to image the very local ground deformation due to earthquakes since there are no benchmarks close to the fault. In contrast the ALOS track 638 dataset covers a short time span (46 days) and accurately shows the ground deformation induced by earthquake along the PFS. Furthermore, on the bases of ALOS-PALSAR interferometric time-series analysis, we found that no significant deformation are detected during the pre-seismic period in the area near the PFS.

For these reasons and in order to have all the datasets (i.e. GPS, leveling and DInSAR) temporally consistent, we scaled the GPS values observed over a ten-month period to a five-month one, corresponding to the leveling and DInSAR ENVISAT time coverage, under the assumption of a linear evolution of the ground deformation pattern through time. The coseismic displacements affected only a narrow area close to the fault, where no GPS benchmarks are present; this let us assume that the GPS network here considered, is not affected by the coseismic displacements but is only sensitive to the constant sliding of the eastern flank of the volcano. We applied the SISTEM integration only on the north-east Mt. Etna area along the PFS (see Fig. 7). In particular, we performed the SISTEM integration on an area of 17,500 × 7550 m with a pixel resolution of 25 m.

The results of the integration are reported in Fig. 7. The 3D components analysis shows a maximum eastward movement (370 mm) associated with maximum relative vertical displacements (70 mm) in a narrow area along the PFS. We performed an analysis of the accuracy, in terms of the estimated standard errors provided by WLS approach. This analysis highlights that it is generally lower than 15, 20 and 12 mm for the east, north and up components respectively, except for some limited areas where the discrepancy between the original data is higher, probably due to local effects (e.g. time difference between GPS survey and SAR passes; higher errors in GPS data, very local deformations, etc.)

In order to better depict the kinematic of the PFS, we show the three cross-sections trending NS (long. 507,000 m UTM) relative to the east, north and up displacement components. The cross sections indicate the strong displacements occurring very close to the PFS and, on its southern side, the widespread ESE-ward motion of the eastern flank of Mt. Etna. Furthermore, the three cross sections highlight the opposite movement of the fault hanging wall (generally trending south) with respect to the footwall, due to the "elastic rebound" of the PFS involved by earthquakes. In the area very close to the fault trace, the north relative components are inverted probably due to a rollback mechanism over a listric fault according to Ruch et al., 2010. This behavior is probably due to the sliding of the eastern flank of Mt. Etna, which moves eastward and gradually stores energy along its northern border (the PFS) in the interseismic period. The northward motion measured on a very narrow strip along the southern side of the fault could be imputable to ruptures occurring on shallow north-dipping antithetic fault planes. When an earthquake occurs, these fault arrangements (semi-graben) locally and temporarily produce a convergent motion towards the PFS, releasing the stretching stress previously stored and snapping back to its original undeformed shape according to Reid's elastic rebound theory (Reid, 1910).

The 3D displacement maps show the kinematics of the PFS well, and are able to also reconstruct the ground deformation affecting the whole investigated area, defining the movements of the north-eastern flank of the volcano.

We highlight here that the deformations detected by SISTEM method are cumulative, and the heterogeneous input data, ranging over a time window longer than coseismic displacement, include the contribution of other earthquakes of the sequence and therefore also the pre- and post seismic ground deformation.

4. Model

We performed data inversion using the high resolution 3D displacement maps provided by SISTEM integration. Since the larger deformation effect is visible along the northwest area of the image, i.e. the area extended 7.5 × 2.5 km along the PFS, it was decided to use only a portion of the whole dataset. This allows simplifying the inversion process and, at the same time, reducing the computational effort. The considered detail image (300 × 100 image with a pixel size = 25 m) is shown in Fig. 8.

We performed an analytical inversion under the assumption of homogeneous, isotropic and elastic half-space by using Okada's model (1985). For the minimization process, we used software based on the GA (Genetic Algorithms) optimization approach as modified by Nunnari et al. (2005). The cost function d assumed is the Index of Agreement as proposed by Nunnari et al. (2005), and is defined according to expression (1):

$$d = \frac{\sum_{i=1}^{N} (P_i - O_i)^2}{\sum_{i=1}^{N} (|P_i - O| + |O_i - O|)^2} \tag{1}$$

Please cite this article as: Guglielmino, F., et al., Analysis of satellite and in situ ground deformation data integrated by the SISTEM approach: The April 3, 2010 earthquake along th..., Earth Planet. Sci. Lett. (2011), doi:10.1016/j.epsl.2011.10.028

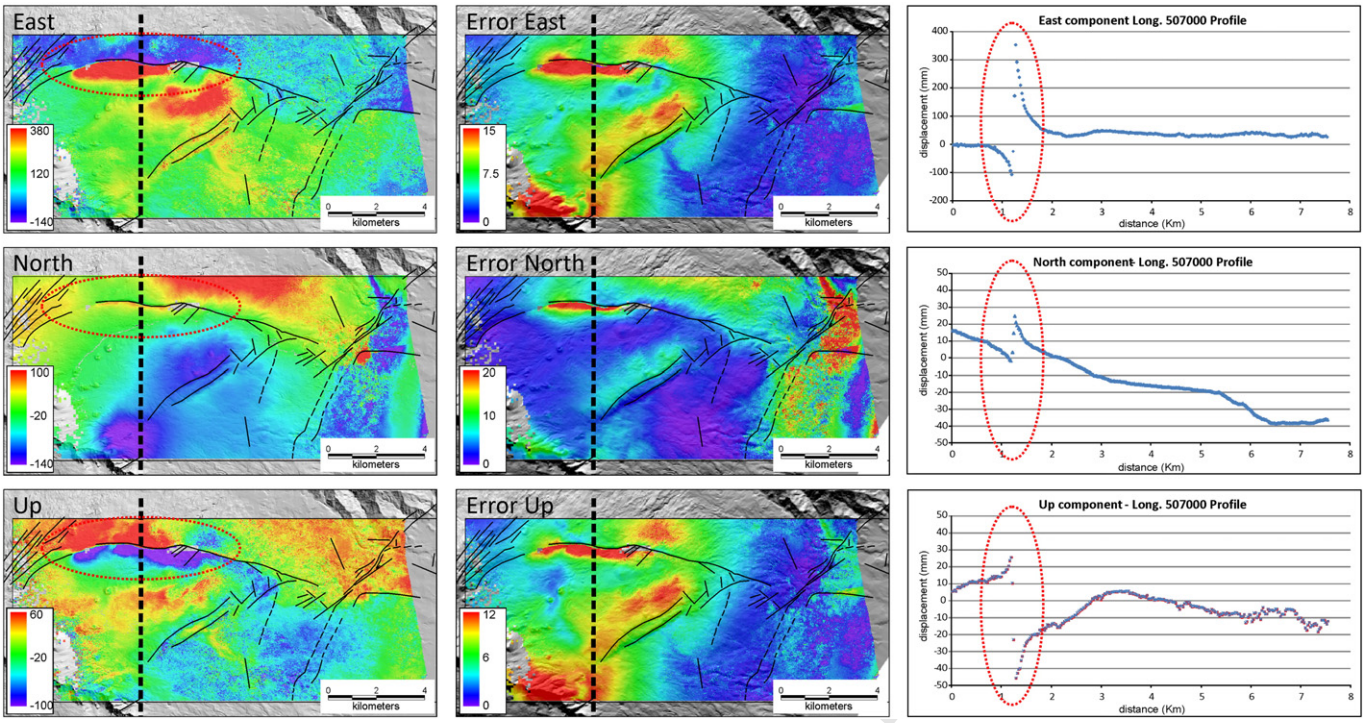

Fig. 7. SISTEM results. In the left column, the three displacement component maps calculated by the SISTEM integration method are reported (for details, see text). The black lines represent the geological structures known from literature. The black dashed lines represent the position of the cross section, and the red ellipses indicate the near field area where the larger deformation effect is visible. In the central column the corresponding estimated standard errors of the east, north, and up components are reported. In the right column, the three cross-sections relative to east, north and up displacement components are reported respectively. All the values are in millimeters.

where N represents the number of measured points, *Oi* and *Pi* indicate the real and predicted values respectively, *O* is the mean values of the real variable.

We inverted our data sets, searching for 5 planar sources together in a homogeneous elastic half space, and the inversion process was performed searching for all parameters of the models without any a priori constraints. In this way, the inversion process was able to search the global minimum by adjusting all parameters of all sources simultaneously.

Each dislocation source in the Okada model is defined by 10 parameters: 3 coordinates of the top center, 2 dimensions of the structure (length and width), its orientation (azimuth and dip angles), and 3 components of displacement (rake, slip and opening) following the Aki and Richards (1980) definition.

The search grid parameters and results of the GA search are summarized in Table 1 and the results of the inversion are shown in Fig. 9. The solution converged to a final fitness value of 92%, and the final result predicting the effect produced by 5 aligned dislocation planes conforms to a left-lateral structure with a mainly maximum slip movement of 65 cm, and an average dipping of 63°S. The model gives a good fit to the data with an average misfit of 1.1, 0.5 and 0.5 cm for east, north and vertical components respectively. The reduced chi-squared χ^2 is equal to 1 considering the a posteriori standard deviation of 2.3, 1.3 and 1.4 cm, for east, north and vertical components respectively, which is of the same order of the average errors (including the errors of the data, the errors of the SISTEM and the incertitude of the model).The expected 3D displacement components fit the integrated SISTEM geodetic data well, producing residuals within ± 5 cm on almost the whole area, except small areas falling in the near field of the fault (i.e. where the deformations are due to a locally more complex secondary fault arrangement). The inversion results provided some first order constraints on the fault and on the phenomenon: (i) faulting is very shallow, it is mainly located between 100 m and 250 m beneath the surface; (ii) the overall orientation (N85E) of ground displacements on the hanging wall produced different amplitude of opening on each dislocation plane, closely related to their azimuth orientation. This means that the western block moves away from the fault trace (this block has a minor azimuth with respect to the ground motion direction) revealing a positive opening component, conversely the other dislocation planes (with an azimuth higher than N85E) reveal a closure component. Bonforte et al. (2007b) have already revealed the increasing inverse

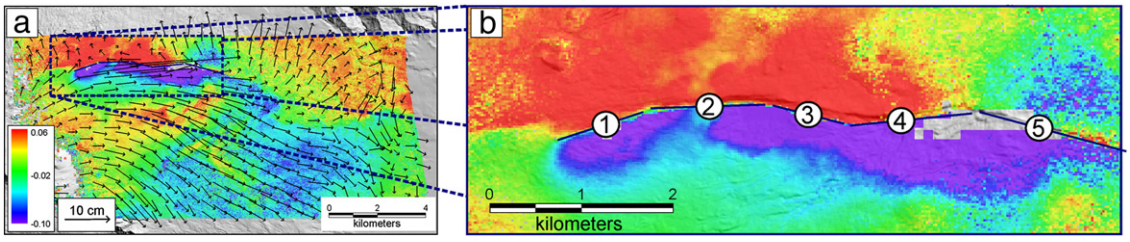

Fig. 8. (a) Displacement vectors and height variations from SISTEM integration. The arrows represent the horizontal displacement vectors, while the vertical displacement is presented by a color map. The dashed-blue rectangle defines the extracted investigated area. (b) Inverted area, the blue lines identify the 5 planar sources searched.

Please cite this article as: Guglielmino, F., et al., Analysis of satellite and in situ ground deformation data integrated by the SISTEM approach: The April 3, 2010 earthquake along th..., Earth Planet. Sci. Lett. (2011), doi:10.1016/j.epsl.2011.10.028

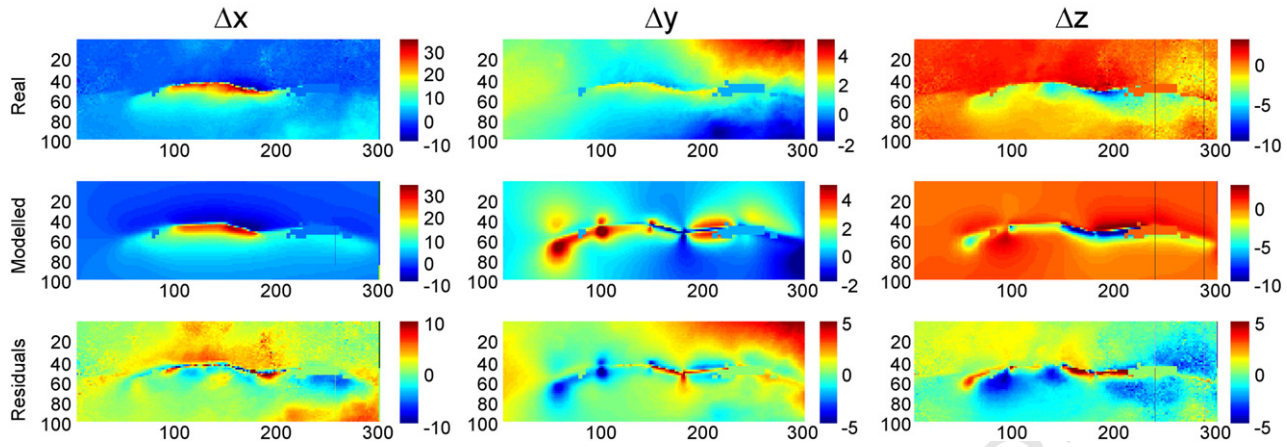

Fig. 9. Inversion results. In the first row are reported the measured Δx, Δy, and Δz components of the displacement field; in the second and third rows the corresponding calculated components, and the residual between measured and modeled displacement values are reported respectively. The values are in mm.

component of displacement on the PFS towards its eastern part, reporting evidence of compressive strain and slight thrusting. along the PFS. They imputed this behavior to the relation between the general eastward motion of the flank of the volcano with the variable azimuth of the fault, ranging from ENE-WSW to ESE-WNW moving from W to E; this rotation of the PFS induces the sliding block to move away from the fault on its western half and to collide with it on its eastern one.

5. Conclusion

The proposed SISTEM method has been satisfactorily applied to study the ground deformation related to the April 2–3 earthquakes that occurred at Mt. Etna.

The SISTEM simultaneously integrates all the available datasets, providing information on ground deformations by taking advantage of the positive features of all these techniques, i.e. the high spatial resolution of DInSAR ENVISAT C-band data, the good coherence of ALOS L-band interferometric data which is also able to detect large gradients of ground deformation, the leveling measurements with sub-mm accuracy, and the 3D displacements component provided by GPS with sub-cm accuracy level.

Furthermore, the availability of geodetic in situ data with lower spatial resolution, coupled with different (ALOS and ENVISAT) and multiple (ascending and descending orbit) SAR data, permitted a detailed integrated high resolution analysis. This enabled us to define the kinematics of PFS and also reconstructing the ground deformation affecting the entire investigated area, identifying the movements of the north-eastern flank of the volcano during a short period characterized by important seismic release.

In particular, the integrated ground deformation field evidenced the strong displacement affecting about 5 km of the fault trace. The kinematics of the fault is confirmed as normal and left-lateral; conversely, while the slip usually occurs only on the southern side of the fault, during this short co-seismic period we measured an evident rebound of the northern side, moving upwards and westwards. The ground deformation field is always asymmetric with much stronger displacements affecting the southern side with respect to the northern one, but it is the first instrumental evidence of an elastic rebound on this fault that decouples a moving flank from a stable one.

Another important aspect coming from the integrated dataset is the areal distribution of the ground displacement. A very strong attenuation of the deformation is evident moving away from the fault. An exceptional displacement of several tens of cm has been detected close to the PFS trace but all datasets testify how this displacement rapidly decreases to a few cm just 1 km away from the fault, and it remains fairly stable over the entire NE flank. This aspect prompted us to hypothesize that the main dynamics is always the seawards sliding of the eastern side of Mt. Etna, which, furthermore, was particularly intense during this period; this general motion deformed and elastically charged a locked portion of the fault that suddenly released the energy by the seismic swarm, recovering its original condition by elastic rebound. All the above considerations would suggest that the earthquake was the result of the movement of the entire north-eastern flank of the volcano rather than its cause.

It should be noted that only the SISTEM integration permitted us to reconstruct the real 3D ground deformation field, allowing overcoming the limitations of each technique and taking advantage of the particular features of each of them. So, we were able to take advantage of the best of each technique, i.e. the fairly continuous spatial sampling of the displacement field (even if 1D) provided by InSAR, the 3D displacements provided by GPS stations (even if on a lower number of points), and the exceptional accuracy of the leveling measurements on a medium-density array that allowed the vertical component of motion to be clearly discriminated from the oblique InSAR views especially in the near field. This was fundamental in a such a displacement field, characterized by very intense and very local ground displacement with an oblique behavior of the fault superimposed on the wider kinematics of the entire north-eastern slope of the volcano.

These results, which provide an accurate spatial characterization of ground deformation, are hence promising for future studies aimed at improving the knowledge about the kinematics of the PFS and the Mt. Etna's unstable flank.

Supplementary materials related to this article can be found online at doi:10.1016/j.epsl.2011.10.028

6. Uncited reference

Okada, 1992

Acknowledgment

The ERS data were provided in the frame of the ESA CAT.1 5843 project. Thanks are due to Giuseppe Brandi, Francesco Calvagna, Salvatore Consoli, Benedetto Saraceno and Gianpiero Aiesi for their essential help in carrying out the leveling and GPS surveys. We thank the Permanent GPS network group for data availability.

This work was partially funded by DPC-INGV Project "Flank", partially by the ASI (SRV Project) and by the Task D7 "Enhancement of the remote sensing laboratory" of the project "Extension and enhancement of the volcanic and seismic monitoring systems of Sicily", funded by the Sicilian regional government.

Please cite this article as: Guglielmino, F., et al., Analysis of satellite and in situ ground deformation data integrated by the SISTEM approach: The April 3, 2010 earthquake along th..., Earth Planet. Sci. Lett. (2011), doi:10.1016/j.epsl.2011.10.028

References

Acocella, V., Neri, M., 2005. Structural features of an active strike–slip fault on the sliding flank of Mt. Etna (Italy). J. Struct. Geol. 27, 343–355.

Aki, K., Richards, P.G., 1980. Quantitative Seismology. Freeman and Co., New York.

Azzaro, R., Ferreli, L., Michetti, A.L., Serva, L., Vittori, E., 1998. Environmental hazard of capable faults: the case of the Pernicana fault (Mt. Etna, Sicily). Nat. Hazards 17, 147–162.

Azzaro, R., Mattia, M., Puglisi, G., 2001. Dynamics of fault creep and kinematics of the eastern segment of the Pernicana fault (Mt. Etna, Sicily) derived from geodetic observations and their tectonic significance. Tectonophys 333, 401–415.

Bonforte, A., Puglisi, G., 2003. Magma uprising and flank dynamics on Mt Etna, studied by GPS data (1992–1994). J. Geophys. Res. 108 (B3), 2153. doi:10.1029/2002JB001845.

Bonforte, A., Puglisi, G., 2006. Dynamics of the eastern flank of Mt. Etna volcano (Italy) investigated by a dense GPS network. J. Volcanol. Geotherm. Res. 153, 357–369. doi:10.1016/j.jvolgeores.2005.12.005.

Bonforte, A., Branca, S., Palano, M., 2007a. Geometric and kinematic variations along the active Pernicana fault: implication for the dynamics of Mount Etna NE flank (Italy). J. Volcanol. Geotherm. Res. 160, 210–222. doi:10.1016/j.jvolgeores.2006.08.009.

Bonforte, A., Gambino, S., Guglielmino, F., Obrizzo, F., Palano, M., Puglisi, G., 2007b. Ground deformation modeling of flank dynamics prior to the 2002 eruption of Mt. Etna. Bull. Volcanol. 69, 757–768. doi:10.1007/s00445-006-0106-1.

Bonforte, A., Bonaccorso, A., Guglielmino, F., Palano, M., Puglisi, G., 2008. Feeding system and magma storage beneath Mt. Etna as revealed by recent inflation/deflation cycles. J. Geophys. Res. 113. doi:10.1029/2007JB005334 B05406.

Bonforte, A., Guglielmino, F., Coltelli, M., Ferretti, A., Puglisi, G., 2011. Structural assessment of Mount Etna volcano from Permanent Scatterers analysis. Geochem. Geophys. Geosyst. 12, Q02002. doi:10.1029/2010GC003213.

Borgia, A., Ferrari, L., Pasquarè, G., 1992. Importance of gravitional spreading in the tectonic and volcanic evolution of Mount Etna. Nature 357, 231–235.

Bousquet, J.C., Lanzafame, G., 2004. The tectonics and geodynamics of Mt. Etna: synthesis and interpretation of geological and geophysical data. In: Bonaccorso, A., Calvari, S., Coltelli, M., Del Negro, C., Falsaperla, S. (Eds.), "Etna Volcano Laboratory", AGU (Geophysical monograph series) (2004), pp. 29–47. doi:10.1029/143GM03.

Branca, S., Coltelli, M., De Beni, E., Wijbrans, J., 2008. Geological evolution f Mt Etna volcano (Italy) from earliest products until the first central volcanism (between 500 and 100 ka ago) inferred from geochronological and stratigraphic data. Int. J. Earth Sci. (Geologische Rundschau) 97, 135–152. doi:10.1007/s00531-006-0152-0.

Corsaro, R.A., Mazzoleni, P., 2002. Textural evidence of peperites inside pillow lavas at Acicastello Castle Rock (Mt. Etna, Sicily). J. Volcanol. Geotherm. Res. 114, 219–229.

Currenti, G., Bonaccorso, A., Del Negro, C., Guglielmino, F., Scandura, D., Boschi, E., 2010. FEM-based inversion for heterogeneous fault mechanisms: application at Etna volcano by DInSAR data. Geophys. J. Int. 183 (2), 765–773. doi:10.1111/j.1365-246X.2010.04769.x.

Goldstein, R.M., Werner, C.L., 1998. Radar interferogram filtering for geophysical applications. Geophys. Res. Lett. 25 (21), 4035–4038.

Gruppo Analisi Dati Sismici, 2010. Terremoti recenti localizzati con la rete sismica della Sicilia Orientale. INGV, Cataniahttp://www.ct.ingv.it/ufs/analisti.

Guglielmino, F., Nunnari, G., Puglisi, G., Spata, A., 2011. Simultaneous and Integrated Strain Tensor Estimation from geodetic and satellite deformation Measurements (SISTEM) to obtain three-dimensional displacement maps. IEEE Trans. Geosci. Remote Sens. vol. 49, 1815–1826. doi:10.1109/TGRS.2010.2103078.

Houlie, N., Briole, P., Bonforte, A., Puglisi, G., 2006. Large scale ground deformation of Etna observed by GPS between 1994 and 2001. Geophys. Res. Lett. 33. doi:10.1029/2005gl024414.

Langer, H., 2010. Rapporto sull'attività sismica in Sicilia orientaleSettimana 29.03.2010 – 04.04.2010, INGV internal report http://www.ct.ingv.it/index.php?option=com_docman&task=doc_view&gid=1761&tmpl=component&format=raw&Itemid=3312010.

Massonnet, D., Feigl, K., 1998. Radar interferometry and its application to changes in the Earth's surface. Rev. Geophys. 36 (4), 441–500.

Neri, M., Acocella, V., Behncke, B., 2004. The role of the Pernicana fault system in the spreading of Mount Etna (Italy) during the 2002–2003 eruption. Bull. Volcanol. 66, 417–430.

Nunnari, G., Puglisi, G., Guglielmino, F., 2005. Inversion of SAR data in active volcanic areas by optimization techniques, Nonlin. Proc. Geophys. 12, 863–870.

Obrizzo, F., Pingue, F., Troise, C., De Natale, G., 2001. Coseismic displacements and creeping along the Pernicana Fault (Etna, Italy) in the last 17 years: a detailed study of a tectonic structure on a volcano. J. Volcanol. Geotherm. Res. 109, 109–131.

Obrizzo, F., Pingue, F., Troise, C., De Natale, G., 2004. Bayesian inversion of 1994–1998 vertical displacements at Mt. Etna: evidence for magma intrusion. Geophys. Jour. Int. 157, 935–946.

Okada, Y., 1992. Internal deformation due to shear and tensile faults in a half-space. Bull. Seismic. Soc. Am. 82 (2), 1018–1040.

Palano, M., Aloisi, M., Amore, M., Bonforte, A., Calvagna, F., Cantarero, M., Consoli, O., Consoli, S., Guglielmino, F., Mattia, M., Puglisi, B., Puglisi, G., 2006. Kinematic and strain analyses of the eastern segment of the Pernicana fault (Mt. Etna, Italy) derived from geodetic techniques (1997–2005). Ann. Geophys. 49 (4–5), 1105–1117.

Puglisi, G., Bonforte, A., 2004. Dynamics of Mount Etna Volcano inferred from static and kinematic GPS measurements. J. Geophys. Res. 109, B11404. doi:10.1029/2003jb002878.

Puglisi, G., Bonforte, A., Ferretti, A., Guglielmino, F., Palano, M., Prati, C., 2008. Dynamics of Mount Etna before, during, and after the July–August 2001 eruption inferred from GPS and differential synthetic aperture radar interferometry data. J. Geophys. Res. 113, B06405. doi:10.1029/2006JB004811.

Reid, H.F., 1910. The Mechanics of the Earthquake, The California Earthquake of April 18, 1906, Report of the State Investigation Commission, Vol. 2. Carnegie Institution of Washington, Washington, D.C.

Romano, R., 1982. Succession of volcanic activity in the Etnean area. In: Romano R (ed) Mount Etna Volcano, a Review of Recent Earth Sciences Studies. Memorie della Società Geologica Italiana 23, 27–48.

Rosen, P.A., Henley, S., Peltzer, G., Simons, M., 2004. Updated Repeat Orbit Interferometry package released. Eos Trans AGU 85 (5), 47.

Ruch, J., Acocella, V., Storti, F., Neri, M., Pepe, S., Solaro, G., Sansosti, E., 2010. Detachment depth revealed by rollover deformation: an integrated approach at Mount Etna. Geophys. Res. Lett. 37. doi:10.1029/2010GL044131 L16304.

Please cite this article as: Guglielmino, F., et al., Analysis of satellite and in situ ground deformation data integrated by the SISTEM approach: The April 3, 2010 earthquake along th..., Earth Planet. Sci. Lett. (2011), doi:10.1016/j.epsl.2011.10.028